Applied Geochemistry 29 (2013) 144–150

Contents lists available at SciVerse ScienceDirect

Applied Geochemistry

journal homepage: www.elsevier.com/locate/apgeochem

Pressure solution of electrically conductive minerals in shallow crust-galvanic processes: A case study from pyrite under differential stress

Qingyou Liu [a], Yanqing Zhang [a,b], Heping Li [a,*]

[a] Laboratory for High Temperature & High Pressure Study of the Earth's Interior, Institute of Geochemistry, Chinese Academy of Sciences, Guiyang 550002, China
[b] Graduate University, Chinese Academy of Sciences, Beijing 100039, China

ARTICLE INFO

Article history:
Received 12 January 2012
Accepted 21 November 2012
Available online 3 December 2012
Editorial handling by K.S. Savage

ABSTRACT

The pressure dissolution behaviour of pyrite was investigated via its polarisation curve and using electrochemical impedance spectroscopy (EIS) in a $FeCl_3$ solution under differential stress. The results showed that the pyrite pressure dissolution process is a galvanic corrosion process and that there is a negative linear relationship between the pyrite potential difference and the stress action. The EIS experiments confirm that the pyrite was in a passive state in a 0.0010 mol L^{-1} $FeCl_3$ solution and that a thin surface layer of $Fe_{1-y}S_2$ was present. In a 0.010 mol L^{-1} $FeCl_3$ solution, the pyrite was in a trans-passive state, in which the aforementioned passive layer became porous. In a 0.10 mol L^{-1} $FeCl_3$ solution, the pyrite was in an active state, the surface layer dissolved completely, and a lattice layer of S_2^0 was created instead of a passive layer of S^0. Under the present stress conditions, the stress action did not change the pyrite electrochemical dissolution mechanism; however, the conditions decreased the charge transfer resistance and passive resistance and increased the species diffusion capacitance.

© 2012 Elsevier Ltd. All rights reserved.

1. Introduction

In geology, pressure solution is defined as the process by which grains dissolve at intergranular and intercrystalline contacts (Tada and Siever, 1989). This phenomenon is a long-standing problem that has engendered continuing arguments with respect to its mechanism, thermodynamic basis, and geological significance. In fact, pressure solution has been used to explain many phenomena in geology, such as stylolitic structure (Guzzetta, 1984; Koehn et al., 2006; Nenna and Aydin, 2011), tectonic accretion (Fueten et al., 2002; Beaumont et al., 2009) and element migration and element activation (Seyfried and Janecky, 1985; Meer et al., 2002; Loring et al., 2004; Birgersson and Karnland, 2009).

In the past few decades, pressure solution has received renewed attention for its important role in the diagenesis of sedimentary rocks and its relationship to rock deformation. Pressure solution has been observed as a fluid migration mechanism (Angevine and Turcotte, 1983), a hydrocarbon accumulation mechanism (Carozzi and Bergen, 1987), and a deformation mechanism under diagenetic conditions (Marshak and Engelder, 1985). Liu and Wu (1994) showed that pressure solution was usually observed as a mechanical–chemical dissolution process. According to the authors' previous research, the above mechanism can sufficiently explain the pressure solution of non-conductive minerals, but conductive minerals, such as metallic sulfides, some oxides and natural metallic minerals, may have a different pressure solution mechanism (Li et al., 1998).

Pyrite, the most abundant sulfide in the Earth's crust (Peters and Majima, 1968), has motivated most of the research in the literature because of its potential use as a component in solar energy collectors (Gerischer, 1975; Chen et al., 1991), depolariser anodes for H_2 production (Lalvani and Shami, 1986), and cathodes in high-energy–density batteries (Vincent et al., 1984). The electrochemical dissolution of pyrite plays an important role in the fields of environmental protection and resource development through phenomena such as the formation of acidic mine drainage (Singer and Stumm, 1970), the biogeochemical cycles of S, Fe and other metals (Nordstrom, 1982), the microbiology of Fe- and S-oxidising bacteria (Sasaki et al., 1994), the mineral processing of sulfides (Murr, 1980), and coal cleaning (Silverman et al., 1961). As a result, there is an extensive literature investigating the dissolution of pyrite that has been published in the past ten years alone (Cabral and Ignatiadis, 2001; Cruz et al., 2001; Chernyshova, 2003, 2004; Lehner et al., 2007; Savage et al., 2008; Liu et al., 2008, 2009b; Heidel and Tichomirowa, 2010).

The authors are not aware of any reports associated with the electrochemical behaviour of pyrite (FeS_2) under stress. However, sulfide minerals under human exploitation or endemic geochemical processes constantly experience stress. For instance, in the Earth's crust, differential stress derived not only from gravitational force, caused by the overlying rocks but also from tectonic, thermal

* Corresponding author.
E-mail address: liheping123@yahoo.com (H. Li).

0883-2927/$ - see front matter © 2012 Elsevier Ltd. All rights reserved.
http://dx.doi.org/10.1016/j.apgeochem.2012.11.006

and other dynamic forces. These differential stresses control the deformation and the fabric variation of rocks (Hast, 1969, 1974). In addition, in the hydrometallurgy field, mechanical activation is often viewed as an effective measure to enhance the leaching processes, needless to say, mechanical action leads to minerals storing residual stress, that is, minerals store the strain energy, which can be converted into electrochemical energy. The strain energy produced by stress can be converted into electrochemical energy, which subsequently influences the electrode potential and electrochemical behaviour of these sulfide minerals, and eventually results in leaching rate enhancement. Ferric chloride ($FeCl_3$) is not only a common electrolyte, it is also the most-used medium for sulfide leaching (Dutrizac, 1992), a common Fe(III) compound in the Earth's crust (Bailey et al., 2002) and a common component of mine waters (Bowell and Bruce, 1995; Silva et al., 2009); consequently, it has a strong influence on the electrochemical behaviour of metal sulfides.

In view of the above discussion, the aim of this work is to study the electrochemical response of pyrite in a $FeCl_3$ solution under differential stress to understand the dissolution kinetics and electrochemical mechanisms. This work will provide the experimental basis for a pressure solution mechanism of pyrite in the shallow crust and will provide the mechanism by which geo-stress affects metal and acidic pollution arising from metal sulfide mine drainage.

2. Experimental methods

2.1. Samples, reagents and instrumentation

Natural pyrite from the Yunfu Fe deposit (Guangdong Province, China) was used in this work. The sample was cut and shaped into a 10 mm × 10 mm × 40 mm block. Within the limits of these techniques, reflected light microscopy and X-ray diffraction analyses indicated that the sample was pure and homogeneous. The electron microprobe analysis indicated that the Fe and S contents (wt%) were 46.89% and 52.96%, respectively. Before the experiments, the electrode surface was polished with metallographic abrasive paper, cleaned with filter paper and then rinsed with acetone. After each experiment, the pyrite electrode was re-polished and re-used.

Analytical grade $FeCl_3$ and double distilled water were used to prepare a series of $FeCl_3$ solutions of various concentrations. During all experiments, a 60 mL electrochemical cell made of rigid polytetrafluoroethylene was filled with $FeCl_3$ solution, without purging the dissolved O_2.

All mineral stress experiments were performed on an electronic universal testing machine controlled by a computer. Two resistance strain gauges were installed on the pyrite sample surface, along the axial and lateral directions. Then, depending on the dynamic and static strain testing systems, axial stress, axial strain and lateral strain data could be obtained. To study the influence of stress, rapid and continuously varying axial stresses (0 Pa; 2.0×10^5 Pa; 4.0×10^5 Pa; 6.0×10^5 Pa) were applied in the electrode potential experiment. The respective polarisation curves and electrical impedance spectroscopy data were collected.

The experiments were conducted using a stationary electrode at an ambient temperature of 25 ± 1 °C.

2.2. Electrode potential measurements under various differential stresses

An Agilent 34410A high-precision digital multimeter connected to a computer was used to measure the electrode potential. A standard two-electrode system with an exposed pyrite area of 4 cm^2 was constructed from a pyrite electrode and a saturated calomel electrode (SCE) connected through a Luggin capillary salt bridge. All potentials recorded in this study were relative to the SCE. The experimental configuration is shown schematically in Fig. 1.

2.3. Polarisation curves and electrical impedance spectroscopy measurements

Polarisation curve measurements were performed using a computer-controlled electrochemical measurement system on a conventional three-electrode electrolytic cell that used Pt as an auxiliary electrode and pyrite as the working electrode. A saturated calomel electrode (SCE) was used as the reference electrode for all electrochemical tests, and all potentials quoted in this study are with respect to the SCE (0.242 V vs. SHE), unless otherwise indicated. The reference electrode was connected to a Luggin capillary to minimise the IR drop. The configuration of the working, auxiliary and reference electrodes were maintained to ensure that each experiment had the same spatial orientation.

The polarisation scan was performed from −250 mV relative to the open circuit potential (E_{OC}) to +250 mV relative to the E_{OC} at a rate of 1 mV/s. Data were recorded after a 60 min immersion in the working solution. The experimental control and data analyses were performed using the PowerCorr software provided by Princeton Applied Research.

The EIS measurements were performed at the open circuit potential in the 1.0×10^4 Hz to 0.1 Hz frequency range using a Parstat-2263 interfaced with a PC. The amplitude of the sinusoidal voltage was 5 mV rms. Data were recorded after a 60 min immersion in the working solution. The equivalent circuit model used for fitting the AC impedance was evaluated with the ZSimpWin (Version 3.10) software from PAR.

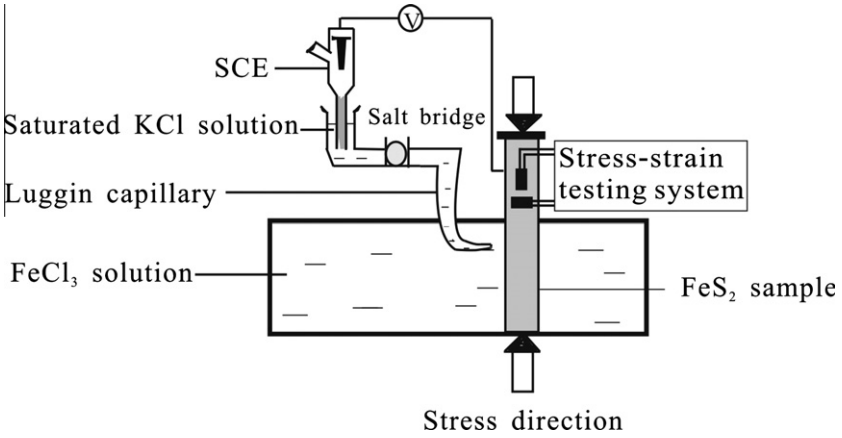

Fig. 1. Schematic diagram showing the stress–potential experimental arrangement.

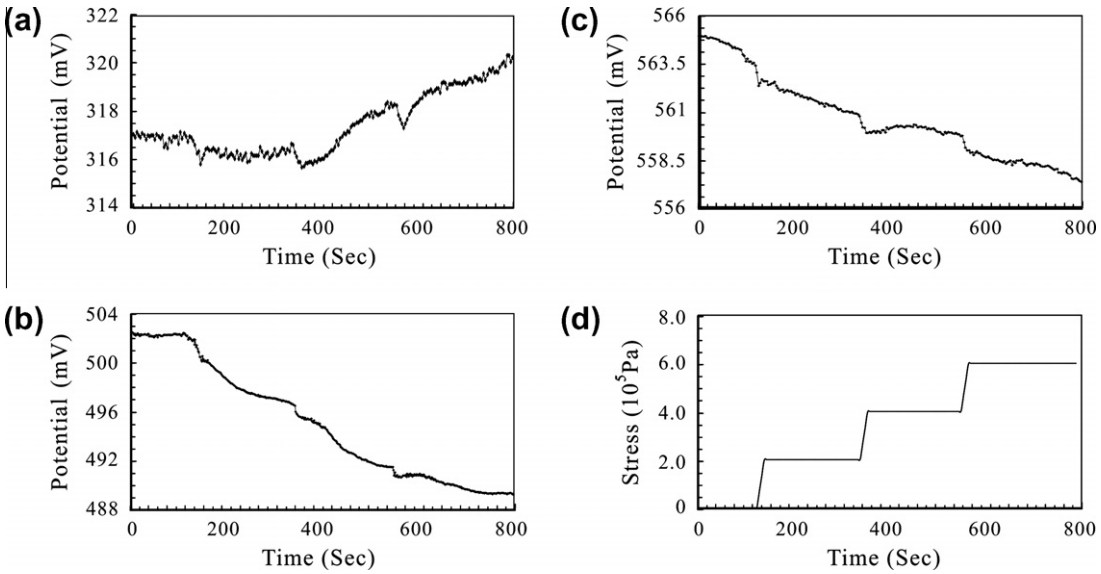

Fig. 2. Variations in pyrite electrode potential under rapid, continuously varying axial stresses (d) in different concentrations $FeCl_3$ solution. (a) 0.0010 mol L^{-1}, (b) 0.010 mol L^{-1} and (c) 0.10 mol L^{-1}.

3. Results and discussion

3.1. Stress, strain and electrode potential

Fig. 2 shows the electrode potentials of pyrite in $FeCl_3$ solutions (0.0010 mol L^{-1}; 0.010 mol L^{-1}; 0.10 mol L^{-1}) under rapid and continuous varying differential stresses. From Fig. 2, it can be seen that the electrode potential of pyrite differed for different $FeCl_3$ solution concentrations under similar differential stresses, but the electrode potential differences remained the same. The combined stress and strain conditions in the experiment allowed for derivation of a stress–strain–potential chart (Fig. 3). From Fig. 3, it can be seen that the axial stress and the axial strain had a positive linear relationship, as did the axial stress and the lateral strain. Both relationships obey Hooke's law. These results indicate that the axial stresses on the pyrite were elastic and that the pyrite experienced elastic strain. From the figure, it can also be seen that the axial stress and the pyrite potential were linked by a negative linear relationship.

The pyrite potential is defined as $\varphi_H^{FeS_2}$. When the pyrite is under elastic stress conditions, mechanical interactions do not affect the electrolyte solution, and the chemical potentials of the reducible ions in the solution do not change, although the chemical potential of the pyrite changes. It can be determined that the electrode potential difference for stress is $\Delta\varphi_H^{FeS_2} = -\frac{VdP}{ZF}$ (Liu et al., 2009a), where V is pyrite molar volume, Z is electron transfer number and F is Faraday constant. This equation shows that there is a negative linear relationship between the pyrite potential difference and the stress action. The experimental results shown in Fig. 2 are consistent with this electrochemical theory.

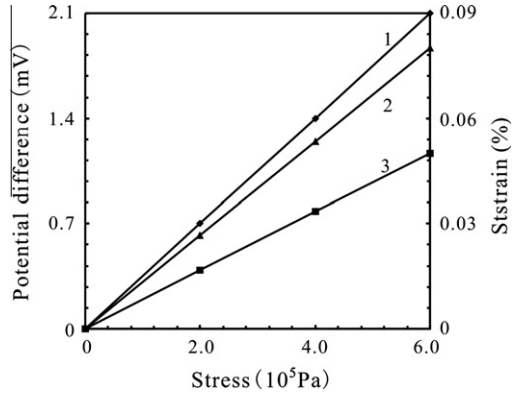

Fig. 3. Chart of pyrite potential difference–stress–strain. (1) axial stress–pyrite potential difference, (2) axial stress–axial strain and (3) axial stress–lateral strain.

3.2. Study of polarisation curves

Fig. 4 shows the Tafel plots for pyrite in naturally aerated $FeCl_3$ solutions (0.0010 mol L^{-1}; 0.010 mol L^{-1}; 0.10 mol L^{-1}). From Fig. 4, it can be seen that increasing stress causes the polarisation curve to shift in the positive direction along the horizontal and longitudinal axes with increasing $FeCl_3$ concentrations. The corrosion current density, the Tafel slope, the transfer coefficient and the number of electrons transferred were calculated according to electrochemical theory (Bard and Faulkner, 2001) using the PAR software.

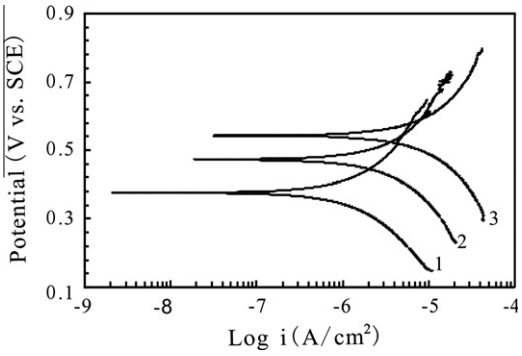

Fig. 4. Tafel plots for pyrite electrode under different concentrations $FeCl_3$ solutions. (1) 0.0010 mol L^{-1}, (2) 0.010 mol L^{-1}, (3) 0.10 mol L^{-1}.

$$I = i_{corr}\left[\exp\frac{2.303(E-E_{corr})}{b_a} - \exp\frac{-2.303(E-E_{corr})}{b_c}\right] \quad (1)$$

$$b_a = \frac{2.303RT}{\beta nF} \quad (2)$$

$$b_c = \frac{2.303RT}{\alpha nF} \tag{3}$$

$$\alpha = 1 - \beta \tag{4}$$

where E_{corr} is corrosion potential; i_{corr} is corrosion current density; b_a and b_c are Tafel slope of anode and cathode, respectively; α and β are transfer coefficient of anode and cathode, respectively; n is number of electron transfer; T is absolute temperature; R is universal gas constant; and F is Faraday constant.

Furthermore, the polarisation resistance values, R_p, can be calculated from the Stern-Geary equation (Gonzalez-Rodriguez et al., 2009):

$$I_{corr} = \frac{b_a b_c}{2.3(b_a + b_c)} \cdot \frac{1}{R_p} \tag{5}$$

The linear polarisation experimental results are listed in Table 1. The pyrite electrode corrosion current density increased from 5.857 to 190.7 μA cm^{-2} as the $FeCl_3$ concentration increased from 0.0010 to 0.10 mol L^{-1}, the corrosion potential became more positive, increasing from 363.161 to 541.407 mV, and the polarisation resistance values decreased from 10.188 to 1.770 Ω cm^2. These results show that increased $FeCl_3$ concentrations promote the pyrite electrochemical interaction and that they induce more significant galvanic corrosion. It should also be noted that the transfer coefficient and the number of electrons transferred, which are indicative of the electrode reaction mechanism (Liu, 2002), changed noticeably at these three different concentrations. These results suggest that there are different electrochemical interaction mechanisms under these conditions. The probable direct cause of this phenomenon is the ability of Cl^- ions to form complexes and compounds with the available Fe ions in the solution. Additionally, the high mobility of the Cl^- ions permits them to reach and coat the electrode surface, halting the formation of oxide and hydroxide films. This action prevents or postpones the neutralisation of the surface (Pavlica, 1974). To further investigate the anode electrochemical mechanism, impedance studies were performed at open circuit potentials for each $FeCl_3$ solution concentration.

3.3. Electrical impedance spectroscopy measurements

Fig. 5a and b shows the Bode and Nyquist plots for the pyrite electrode in 0.0010 mol L^{-1} $FeCl_3$ solution under different elastic axial stresses. The results show that they have similar Bode and Nyquist profiles. This similarity shows that the pyrite electrode has the same electrochemical interaction mechanism under these differing axial stresses (0; 2.0×10^5 Pa; 4.0×10^5 Pa; 6.0×10^5 Pa). As the stress increases, the total impedance magnitude of the system decreases, and the phase angle decreases for high frequencies and increases for the low frequencies. An examination of the Bode plots in Fig. 5a reveals there are two time constants corresponding to two faradaic relaxation processes. The first time constant, which is observed at high frequencies, is a capacitive loop that is related to the charge transfer resistance from the electrochemical dissolution of the electrode. The second time constant, which occurs at the middle-high frequencies, is another a capacitive loop that is related to the combination of the pseudo-capacitive impedance of the passive layer and a resistance. Consequently, the equivalent circuit shown in Fig. 5c was employed to fit the experimental impedance data. In the equivalent circuit, R_s represents resistances from the electrolyte and other ohmic sources in their respective electrochemical circuits, CPE_t is the constant phase element that corresponds to the double-layer capacitance, R_t is the charge transfer resistance, and the CPE_p/R_p pair represents the capacitive and resistive behaviours of the passive film. Under these conditions, the film is believed to be composed of $Fe_{1-y}S_2$ and created by the following reaction (Karthe et al., 1993).

$$FeS_2 \rightarrow Fe_{1-x}S_2 + xFe^{2+} \tag{6}$$

The impedance of the *CPE* is given by Macdonald (1985):

$$Z_{CPE} = \frac{1}{Y_0(j\omega)^n} \tag{7}$$

Here, Z_{CPE} is the impedance of the constant phase element (Ω cm^2), ω is the angular frequency of the AC voltage (rad s^{-1}), Y_0 is the magnitude of admittance of the *CPE* (Ω^{-1} cm^{-2} S^{-n}) and n is the exponential term. The values associated with the different elements in the equivalent circuit are shown in Table 2. It can be observed that the space charge transform resistance R_t decreased from 4942 to 2143 Ω cm^2 and that the passive film resistance R_p decreased from 5.011E4 to 1.198E4 Ω cm^2 when the stress increased from 0 to 6.0×10^5 Pa. The Y_0 value of the CPE_t increased from 6.758E−7 to 9.167E−5, and Y_0 of the CPE_p increased from 7.635E−4 to 8.838E−4. In the cases above, the two Y_0 values refer to the double-layer and passive film capacitances, respectively. These capacitances are related to the pyrite dissolution and passive film depletion processes, respectively. A higher Y_0 value indicates an increased transport of ions through the double-charge layer and the passive layer. The high capacitance and low resistance of the films on the specimens indicate the relatively poor robustness of the passive film. These results reveal that greater stresses enhance pyrite pressure dissolution and passive film depletion.

As the concentration of the $FeCl_3$ solution increases, the pyrite open circuit potential increases, and the existing passive layer is oxidised and becomes increasingly porous to the strong penetrative nature of the Cl^- ions. Fig. 6 shows the Bode plot diagram and a typical Nyquist diagram for pyrite in the presence of a 0.010 mol L^{-1} $FeCl_3$ solution under different elastic axial stresses. The Bode and Nyquist plots at this concentration have similar profiles to the 0.0010 mol L^{-1} result for different axial stresses, revealing the same corrosion pattern. Furthermore, Fig. 6a and b shows two obvious time constants, as indicated by two distorted capacitive loops. Fig. 6c shows the equivalent circuit employed to fit the experimental data, where R_s describes the electrolytic and other ohmic resistances in the respective electrochemical circuits, and the CPE_t/R_t pair represents the charge transform capacitive and resistive behaviours in the space charge region, respectively. The pair CPE_1/R_1 refers to sections of the passive layer with the maximum thickness and the C_p/R_p pair refer to sections of the passive layer with the minimum thickness (Mansfeld and Kendig, 1988). The constant phase element *CPE* is used to account for the capacitance, which probably arises from electrode surface defects. The values of the different elements in the equivalent circuit are shown in Table 3. The results in Table 3 are for the case when the elastic

Table 1
Electrochemical kinetic parameters of the FeS_2 samples from Tafel tests.

$FeCl_3$ (mol L^{-1})	E_{corr} (mV)	i_{corr} (μA cm^{-2})	b_a (mV)	b_c (mV)	α	β	n	R_p (Ω cm^2)
0.0010	363.161	5.857	236.066	327.861	0.419	0.581	0.0518	10.188
0.010	458.317	51.18	678.283	1612.299	0.296	0.704	0.148	4.056
0.10	541.407	190.7	1286.320	1958.020	0.396	0.604	0.914	1.770

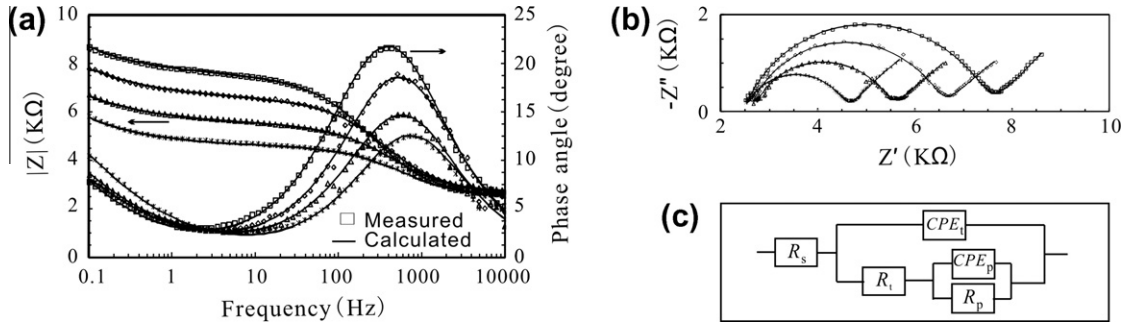

Fig. 5. Bode plots and phase angles (a), Nyquist impedance spectra (b) and equivalent circuit (c) for pyrite under differential stresses in 0.0010 mol L^{-1} $FeCl_3$ solutions. (□) 0 Pa, (◇) 2.0×10^5 Pa, (Δ) 4.0×10^5 Pa and (×) 6.0×10^5 Pa.

Table 2
Impedance parameters of FeS_2 in 0.0010 mol L^{-1} $FeCl_3$ solutions under differential stresses.

$FeCl_3$ (mol L^{-1})	Stress (10^5 Pa)	CPE_t, Y_0 (S cm^{-2} s^{-n})	n	R_t (Ω cm^2)	CPE_p, Y_0 (S cm^{-2} s^{-n})	n	R_p (Ω cm^2)
0.0010	0	6.758E−7	0.8107	4942	7.635E−4	0.5026	5.011E4
	2	6.894E−7	0.8017	3885	8.037E−4	0.4873	4.189E4
	4	8.070E−5	0.7867	2821	8.247E−4	0.4652	1.680E4
	6	9.167E−5	0.7716	2143	8.838E−4	0.4613	1.198E4

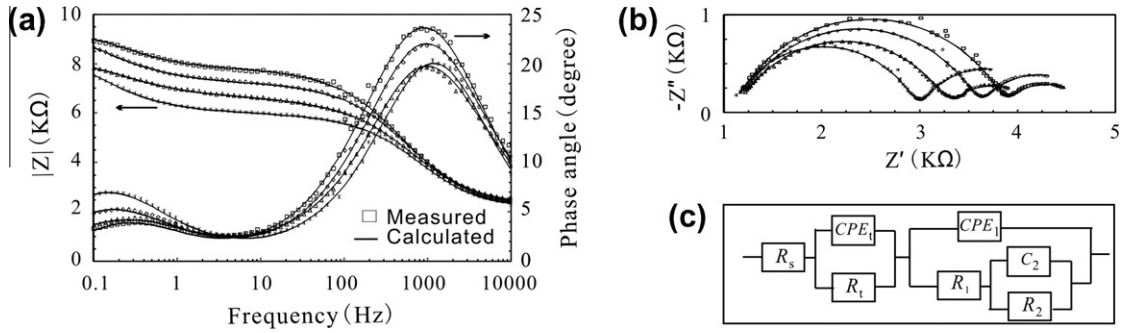

Fig. 6. Bode plots and phase angles (a), Nyquist impedance spectra (b) and equivalent circuit (c) for pyrite under differential stresses in 0.010 mol L^{-1} $FeCl_3$ solutions. (□) 0 Pa, (◇) 2.0×10^5 Pa, (Δ) 4.0×10^5 Pa and (×) 6.0×10^5 Pa.

Table 3
Impedance parameters of FeS_2 in 0.010 M $FeCl_3$ solutions under differential stresses.

$FeCl_3$ (mol L^{-1})	Stress (10^5 Pa)	CPE_t, Y_0 (S cm^{-2} s^{-n})	n	R_t (Ω cm^2)	CPE_1, Y_0 (S cm^{-2} s^{-n})	n	R_1 (Ω cm^2)	C_2 (F cm^{-2})	R_2 (Ω cm^2)
0.010	0	1.179E−3	0.7568	2692	9.773E−7	0.7541	4.653E4	4.746E−6	3019
	2	1.426E−3	0.6037	2170	9.829E−7	0.7544	3.396E4	1.420E−5	2714
	4	1.627E−3	0.7615	1984	1.002E−6	0.7732	1.322E4	3.640E−5	2254
	6	1.857E−3	0.7776	1791	8.993E−5	0.6910	7.871E3	9.109E−5	1479

stresses are increased from 0 to 6.0×10^5 Pa and are summarised as follows: (1) the charge transfer resistance decreases from 2692 to 1791 Ω cm^2, and the capacitance parameter increases from 1.179E−3 to 1.857E−3 S cm^{-2} s^{-n}; (2) the resistance of sections of the passive layer with the maximum thickness decreases from 4.653E4 to 7.871E3 Ω cm^2, and the capacitance parameter increases from 9.773E−7 to 8.993E−5 S cm^{-2} s^{-n}; and (3) the resistance of sections of the passive layer with the minimum thickness decreases from 3019 to 1479 Ω cm^2, and the capacitance value increases from 4.746E−6 to 9.109E−5 F cm^{-2}. These results demonstrate the following trends: (1) the charge transfer resistance decreases and the double layer capacitance parameter increases as the pyrite stress increases, which indicates that stress promotes pyrite dissolution; (2) the resistance of the passive layer in sections with the maximum/minimum thicknesses decreases as the stress increases, whereas the capacitance value of sections of the passive layer with the maximum/minimum thicknesses increases. These trends reveal that stress enhances passive pitting corrosion.

As the concentration of the $FeCl_3$ solution increases, open circuit potential and corrosion potential of the pyrite increase. Fig. 7a and b presents the Bode and Nyquist plots, respectively, for the pyrite electrode in the 0.10 mol L^{-1} $FeCl_3$ solution under different elastic axial stresses. The similarity of these plots reveals that the same electrochemical mechanism occurs under different values of stress. However, Fig. 7a and b do not exhibit a clear capacitive loop in the low frequency range. It can be concluded that a passive film was not present with a high concentration of Cl^- ions. This outcome could be explained by the mechanism proposed by Ahlberg and Broo (1997): in this potential region, the initial oxidation proceeds

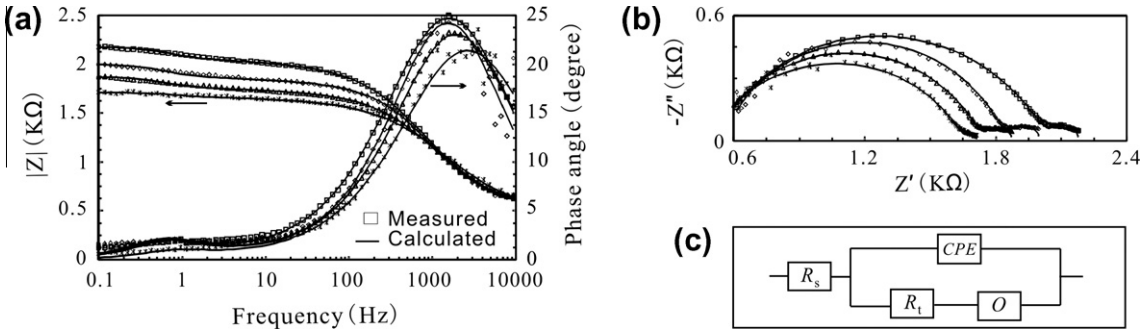

Fig. 7. Bode plots and phase angles (a), Nyquist impedance spectra (b) and equivalent circuit (c) for pyrite under differential stresses in 0.10 mol L^{-1} $FeCl_3$ solutions. (□) 0 Pa, (◇) 2.0×10^5 Pa, (Δ) 4.0×10^5 Pa and (×) 6.0×10^5 Pa.

Table 4
Impedance parameters of FeS_2 in 0.10 M $FeCl_3$ solutions under differential stresses.

$FeCl_3$ (mol L^{-1})	Stress (10^5 Pa)	*CPE*, Y_0 (S cm^{-2} s^{-n})	*n*	R_t (Ω cm^2)	Coth, Y_0 (S cm^{-2} $s^{-0.5}$)	*B* ($s^{-0.5}$)
0.10	0	8.262E−7	0.7606	1307	4.280E−3	0.8356
	2	8.537E−7	0.8082	1275	4.699E−3	0.7892
	4	1.377E−6	0.7402	1246	6.714E−3	0.7091
	6	1.640E−6	0.7061	1171	7.424E−3	0.6762

without destruction of the lattice. The electrons involved possess energy levels of both Fe and the lattice layer S_2^0, as indicated by reaction (7). The presence of S_2^0 instead of S^0 indicates that elemental S may not be formed, so it is not obvious that a passive product is created.

$$FeS_2 \rightarrow Fe^{3+} + S_2^0 + 3e^- \quad (8)$$

The equivalent electrical circuit shown in Fig. 7c was used to fit the experimental data, where R_s describes the electrolytic and other ohmic resistances in the respective electrochemical circuits. The time constant in the high-frequency region is the fast charge transfer process between the pyrite and the Fe^{3+} species. R_t is the charge transfer resistance. A constant phase element (*CPE*) was substituted for the double-layer capacitance connection of the Helmholtz layer and the surface film. The Warburg element *O* represents the Fe^{3+} species diffusion process, which describes dimensional diffusion through a layer of finite thickness. From an electrical perspective, this representation is equivalent to the impedance of a transmission line of finite length. The different model parameters are shown in Table 4. The following changes were observed when the elastic stress increased from 0 to 6.0×10^5 Pa: the charge transfer resistance decreased from 1307 to 1171 Ω cm^2; the capacitance parameter increased from 8.262E−7 to 1.640E−6 S cm^{-2} s^{-n}; the capacitance parameter (coth) increased from 4.280E−3 to 7.424E−3 S cm^{-2} s^{-n}; and the time constant decreased from 0.8356 to 0.6762 $s^{-0.5}$. These results show the following: (1) similar to the previous results, stress promotes pyrite pressure dissolution; (2) increasing stress causes the capacitance parameter (coth) to increase and the time constant to decrease, which indicates stress-enhanced dimensional Fe^{3+} diffusion through a layer of finite thickness.

4. Conclusions

The pressure dissolution behaviour of pyrite (FeS_2) in a $FeCl_3$ solution under differential stress has been studied using polarisation curves and electrical impedance spectroscopy. The following conclusions can be drawn:

(1) For electrically conductive minerals (such as pyrite) in the shallow crust, when an electrolyte is present, their pressure dissolution process is a galvanic corrosion process.
(2) There is a negative linear relationship between the pyrite potential difference and the stress action, and the potential is only affected by the characteristics of the mineral. The mathematical expression is the following: $\Delta\varphi_H^{FeS_2} = -\frac{VdP}{ZF}$.
(3) Different transfer coefficients and numbers of electrons transferred reveal that pyrite has different electrochemical dissolution mechanisms in 0.0010 mol L^{-1}, 0.010 mol L^{-1} and 0.10 mol L^{-1} $FeCl_3$ solutions. Furthermore, increasing the concentration of the $FeCl_3$ solution enhances pyrite electrochemical dissolution.
(4) EIS experiments confirmed the different dissolution mechanisms of pyrite. In a 0.0010 mol L^{-1} $FeCl_3$ solution, the pyrite is in a passive state, and a thin surface layer of $Fe_{1-y}S_2$ is present. In a 0.010 mol L^{-1} $FeCl_3$ solution, the pyrite is in a trans-passive state, and the aforementioned passive layer becomes porous. In a 0.10 mol L^{-1} $FeCl_3$ solution, the pyrite is in an active state. The surface layer is completely dissolved, and a lattice layer S_2^0 is created instead of a passive layer S^0. Under the experimental conditions, the stress action did not change the pyrite electrochemical dissolution mechanism. However, in all stress experiments, the stress action decreased the charge transfer resistance and the passive resistance. Additionally, the stress action increased the species diffusion capacitance by significantly enhancing the ionic transport and diffusion processes.

Acknowledgments

This work was financially supported by National Natural Science Foundation of China (40803017), Large-scale Scientific Apparatus Development Program of Chinese Academy of Sciences (YZ200720), and 135 Program of the Institute of Geochemistry, CAS, Key Technologies R&D Program of Guizhou Province, China (SY [2011] 3088), and Ocean 863 Program (2010AA09Z207) of the Ministry of Science and Technology, China.

References

Ahlberg, E., Broo, A.E., 1997. Electrochemical reaction mechanisms at pyrite in acidic perchlorate solutions. J. Electrochem. Soc. 144, 1281–1285.
Angevine, C.L., Turcotte, D.L., 1983. Porosity reduction by pressure solution: a theoretical model for quartz arsenates. Geol. Soc. Am. Bull. 94, 129–134.

Bailey, R.A., Clark, H.M., Ferris, J.P., Krause, S., Strong, R.L., 2002. The Earth's Crust Chemistry of the Environment, second ed. Academic Press, Elsevier, pp. 443–482.

Bard, A.J., Faulkner, L.R., 2001. Electrochemical Methods Fundamentals and Applications, second ed. John Wiley, New York, pp. 87–136.

Beaumont, C., Jamieson, R.A., Butler, J.P., Warren, C.J., 2009. Crustal structure: a key constraint on the mechanism of ultra-high-pressure rock exhumation. Earth Planet. Sci. Lett. 287, 116–129.

Birgersson, M., Karnland, O., 2009. Ion equilibrium between montmorillonite interlayer space and an external solution—consequences for diffusional transport. Geochim. Cosmochim. Acta 73, 1908–1923.

Bowell, R.J., Bruce, I., 1995. Geochemistry of iron ocher's and mine waters from Levant Mine, Cornwall. Appl. Geochem. 10, 237–250.

Cabral, T., Ignatiadis, I., 2001. Mechanistic study of the pyrite–solution interface during the oxidative bacterial dissolution of pyrite (FeS_2) by using electrochemical techniques. Int. J. Miner. Process. 62, 41–64.

Carozzi, A.V., Bergen, V.D., 1987. Stylolitic porosity in carbonates: a critical factor for deep hydrocarbon production. J. Pet. Geol 10, 267–282.

Chen, G.C., Zen, J.M., Fan, F.R.F., Bard, A.J., 1991. Electrochemical investigation of the energetics of irradiated FeS_2 (pyrite) particles. J. Phys. Chem. 95, 3682–3687.

Chernyshova, I.V., 2003. An in situ FTIR study of galena and pyrite oxidation in aqueous solution. J. Electroanal. Chem. 558, 83–98.

Chernyshova, I.V., 2004. Pyrite oxidation mechanism in aqueous solutions: an in situ FTIR study. Russ. J. Electrochem. 40, 69–77.

Cruz, R., Bertrand, V., Monroy, M., Gonzalez, I., 2001. Effects of sulfide impurities on the reactivity of pyrite and pyritic concentrates: a multi-tool approach. Appl. Geochem. 16, 803–819.

Dutrizac, E.J., 1992. The leaching of sulphide minerals in chloride media. Hydrometallurgy 29, 1–45.

Fueten, F., Robin, P.F., Schweinberger, M., 2002. Finite element modelling of the evolution of pressure solution cleavage. J. Struct. Geol. 24, 1055–1064.

Gerischer, H., 1975. Electrochemical photo and solar cells—principles and some experiments. J. Electroanal. Chem. 58, 265.

Gonzalez-Rodriguez, J.G., Mejia, E., Lucio-Garcia, M.A., Salinas-Bravo, V.M., Porcayo-Calderon, J., Martinez-Villaf, A., 2009. An electrochemical study of the effect of Li on the corrosion behavior of Ni_3Al intermetallic alloy in molten (Li + K) carbonate. Corros. Sci. 51, 1619–1627.

Guzzetta, G., 1984. Kinematics of stylolite formation and physics of the pressure-solution process. Tectonophysics 101, 383–394.

Hast, H., 1969. The state of stress in the upper part of the Earth's crust. Tectonophysics 8, 169–211.

Hast, H., 1974. The state of stress in the upper part of the Earth's crust as determined by measurements of absolute rock stress. Naturwissenschaften 61, 468–475.

Heidel, C., Tichomirowa, M., 2010. The role of dissolved molecular oxygen in abiotic pyrite oxidation under acid pH conditions – experiments with ^{18}O-enriched molecular oxygen. Appl. Geochem. 25, 1664–1675.

Karthe, S., Szargan, R., Suoninen, E., 1993. Oxidation of pyrite surfaces: a photoelectron spectroscopic study. Appl. Surf. Sci. 72, 157–170.

Koehn, D., Malthe-Sørenssen, A., Passchier, C.W., 2006. The structure of reactive grain-boundaries under stress containing confined fluids. Chem. Geol. 230, 207–219.

Lalvani, S.B., Shami, M.J., 1986. Electrochemical oxidation of pyrite slurries. J. Electrochem. Soc. 133, 1364–1368.

Lehner, S., Savage, K., Ciobanu, M., David, E., Cliffel, D.E., 2007. The effect of As, Co., and Ni impurities on pyrite oxidation kinetics: an electrochemical study of synthetic pyrite. Geochim. Cosmochim. Acta 71, 2491–2509.

Li, H.P., He, S.X., Xie, H.S., Peng, E.S., Zhang, Z.R., 1998. A new mechanism for pressure solution of electrically conductive minerals in shallow crust: a process of stress galvanic cell. Acta Mineral. Sin. 18, 80–83 (in Chinese with English abstract).

Liu, J.S., 2002. Bioextraction and Corrosion Electrochemistry of Sulfide Minerals. Ph.D. Thesis, Central South University, pp. 34–38.

Liu, L.M., Wu, Y.Z., 1994. Mechanical–chemical interactions during mobilized mineralization of disperse elements in metamorphic rocks. Geol. Sci. Technol. Inf. 13 (4), 59–64 (in Chinese with English abstract).

Liu, R., Wolfe, A.L., Dzombak, D.A., Horwitz, C.P., Stewart, B.W., Capo, R.C., 2008. Electrochemical study of hydrothermal and sedimentary pyrite dissolution. Appl. Geochem. 23, 2724–2734.

Liu, Q.Y., Li, H.P., Zhou, L., 2009a. Experimental study of pyrite-galena galvanic in a flowing system and its applied implications. Hydrometallurgy 96, 132–139.

Liu, R., Wolfe, A.L., Dzombak, D.A., Horwitz, C.P., Stewart, B.W., Capo, R.C., 2009b. Controlled electrochemical dissolution of hydrothermal and sedimentary pyrite. Appl. Geochem. 24, 836–842.

Loring, J., Yu, P., Phillips, B.L., Casey, W.H., 2004. Activation volumes for oxygen exchange between the $GaO_4Al_{12}(OH)_{24}(H_2O)_{12}^{7+}(aq)$ ($GaAl_{12}$) polyoxocation and aqueous solution from variable pressure ^{17}O NMR spectroscopy. Geochim. Cosmochim. Acta 68, 2791–2798.

Macdonald, J.R., 1985. Generalizations of "universal dielectric response" and a general distribution-of-activation-energies model for dielectric and conducting systems. J. Appl. Phys. 58, 1971–1978.

Mansfeld, F., Kendig, M.W., 1988. Evaluation of anodized aluminum surfaces with electrochemical impedance spectroscopy. J. Electrochem. Soc. 135, 828–833.

Marshak, S., Engelder, T., 1985. Development of cleavage in limestones of a fold thrust belt in eastern New York. J. Struct. Geol. 7, 345–359.

Meer, S.D., Spiers, C.J., Peach, C.J., Watanabe, T., 2002. Diffusive properties of fluid-filled grain boundaries measured electrically during. Earth Planet. Sci. Lett. 200, 147–157.

Murr, L.E., 1980. Theory and practice of copper sulfide leaching in dumps and in-situ. Miner. Sci. Eng. 12, 12–189.

Nenna, F., Aydin, A., 2011. The role of pressure solution seam and joint assemblages in the formation of strike-slip and thrust faults in a compressive tectonic setting; The Variscan of south-western Ireland. J. Struct. Geol. 33, 1595–1610.

Nordstrom, D.K., 1982. Aqueous pyrite oxidation and the consequent formation of secondary iron minerals. In: Hossaer, L.R., Kittrick, J.A., Faming, D.F. (Eds.), Acid Sulfate Weathering. Soil Science Soc. Am., vol. 42, pp. 48–50 (Chapter 3).

Pavlica, J.J., 1974. Electrochemistry of Pyrrhotite in Flotation. M.S. Thesis, Univ. Minnesota.

Peters, E., Majima, H., 1968. Electrochemical reactions of pyrite in acid perchlorate solutions. Can. Metall. Q. 7, 111–117.

Sasaki, K., Konno, H., Inagaki, M., 1994. Structural strain in pyrites evaluated by X-ray powder diffraction. J. Min. Mater. Process. Inst. Jpn. 29, 1666–1669.

Savage, K.S., Stefan, D., Lehner, S.W., 2008. Impurities and heterogeneity in pyrite: influences on electrical properties and oxidation products. Appl. Geochem. 23, 103–120.

Seyfried, J.W.E., Janecky, D.R., 1985. Heavy metal and sulfur transport during subcritical and supercritical hydrothermal alteration of basalt: influence of fluid pressure and basalt composition and crystallinity. Geochim. Cosmochim. Acta 49, 2545–2560.

Silva, E.F.D., Bobos, I., Matos, J.X., Patinha, C., Reis, A.P., Fonseca, E.C., 2009. Mineralogy and geochemistry of trace metals and REE in volcanic massive sulfide host rocks, stream sediments, stream waters and acid mine drainage from the Lousal mine area (Iberian Pyrite Belt, Portugal). Appl. Geochem. 24, 383–401.

Silverman, M.P., Rogoff, M.H., Wender, I., 1961. Bacterial oxidation of pyritic materials in coal. Appl. Microbiol. 9, 491–496.

Singer, P.C., Stumm, W., 1970. Acidic mine drainage, the rate-determining step. Science 167, 1121–1123.

Tada, R., Siever, R., 1989. Pressure solution during diagenesis. Ann. Rev. Earth Planet. Sci. 17, 89–118.

Vincent, C.A., Bonino, F., Lazzari, M., Scrosati, B., 1984. Modern Batteries: An Introduction to Electrochemical Power Sources. Edward Arnold Ltd., London.